Methods for Kinetic Modeling of Temporally Resolved Hyperspectral Confocal Fluorescence Images

PATRICK J. CUTLER, DAVID M. HAALAND, ERIK ANDRIES, and PAUL J. GEMPERLINE*

Department of Chemistry, East Carolina University, Greenville, North Carolina 27858 (P.J.C., P.J.G.); Sandia National Laboratories, Albuquerque, New Mexico 87185-0895 (D.M.H.); and Department of Mathematics and Pathology, University of New Mexico, Albuquerque, New Mexico 87131 (E.A.)

Elucidating kinetic information (rate constants) from temporally resolved hyperspectral confocal fluorescence images offers some very important opportunities for the interpretation of spatially resolved hyperspectral confocal fluorescence images but also presents significant challenges, these being (1) the massive amount of data contained in a series of time-resolved spectral images (one time course of spectral data for each pixel) and (2) unknown concentrations of the reactants and products at time = 0, a necessary precondition normally required by traditional kinetic fitting approaches. This paper describes two methods for solving these problems: direct nonlinear (DNL) estimation of all parameters and separable least squares (SLS). The DNL method can be applied to reactions of any rate law, while the SLS method is restricted to first-order reactions. In SLS, the inherently linear and nonlinear parameters of first-order reactions are solved in separate linear and nonlinear steps, respectively. The new methods are demonstrated using simulated data sets and an experimental data set involving photobleaching of several fluorophores. This work demonstrates that both DNL and SLS hard-modeling methods applied to the kinetic modeling of temporally resolved hyperspectral images can outperform traditional soft-modeling and hard/soft-modeling methods which use multivariate curve resolution–alternating least squares (MCR-ALS) methods. In addition, the SLS method is much faster and is able to analyze much larger data sets than the DNL method.

Index Headings: Hyperspectral confocal microscopy; Fluorescence imaging; Photobleaching; Kinetic modeling; Hard modeling; Soft modeling; Multivariate curve resolution; MCR; Separable least squares; SLS; Direct nonlinear estimation; DNL.

INTRODUCTION

Hyperspectral confocal fluorescence imaging is a newly developed technology with many promising advantages over filter-based confocal fluorescence imaging. The development of filter-based confocal fluorescence microscopes enabled scientists to monitor biological samples with several fluorescently tagged stains or proteins in living cells. However, filter-based instruments are limited in the number of fluorescent tags that can be resolved simultaneously because of their limited spectral resolution. Hyperspectral confocal microscopy can be used to overcome these limitations by acquiring higher spectral resolution at hundreds of wavelength channels for each pixel or voxel in the image and by using chemometric methods for subsequent mathematical resolution of multiple overlapping fluorophores. Massive data sets (e.g., 200 pixels $\times$ 200 pixels $\times$ 512 wavelength channels per pixel $\times$ 18 time points) can be produced in a single experiment at a rate of 8300 spectra per second.[1] When represented as 8 bytes per point for floating point calculations, these large image data sets (3 Gbytes each) can pose significant challenges to chemometric data processing methods.

Three types of multivariate modeling algorithms are discussed in this work: soft-modeling, hard-modeling, and hard/soft-modeling algorithms. Soft-modeling algorithms, such as multivariate curve resolution–alternating least squares (MCR-ALS), are very useful for estimating physically relevant pure-component concentration profiles and their corresponding pure-component spectra with very little or no *a priori* knowledge.[2] One drawback of this approach is that little information about the underlying mechanism of time-dependent change in the system is revealed. Hard-modeling techniques, such as kinetic modeling, are very useful for estimating time-dependent concentration profiles of a system that can be described by first-principle physical models, but they have the limitation that all components in the system must strictly follow the proposed reaction mechanism.[3–6] Hard/soft-modeling is a hybrid of soft-modeling and hard-modeling methods. It allows the concentration profile of some of the individual species to be constrained to follow a proposed mechanism while allowing greater flexibility in the shapes of time-dependent concentration profiles for the remaining components.[7–9] Although rate constants can be roughly estimated from soft-model-derived concentration profiles by directly fitting a model-based curve to the time-resolved concentrations, the hard/soft-modeling and hard-modeling techniques employed in this work introduce kinetic models into the modeling algorithm in order to obtain more accurate estimates of rate constants and to reduce rotational ambiguities[10] associated with soft-modeling techniques.

Existing multivariate hard-modeling techniques have been utilized in numerous kinetic applications including monitoring and controlling batch processes,[11–13] modeling of the complexation kinetics of metals,[14–18] and modeling solvent-free organic reactions.[19]

In existing multivariate hard-modeling techniques, the concentrations of all species at time zero (t_0) in the postulated model must be known. In some applications, it is not possible to know the initial concentrations (concentrations at t_0) of all species in a given system. For example, in a hyperspectral fluorescence microscope image of a biological specimen with fluorescently labeled proteins or stains, it is very unlikely that the initial concentrations of all fluorescing species will be known. Thus, in order to kinetically model these types of systems using hard-modeling, new techniques must be developed.

Two hard-modeling techniques have been developed in this investigation for systems with unknown initial concentrations (e.g., temporally resolved hyperspectral fluorescence images): (1) direct nonlinear fitting (DNL) and (2) separable least squares fitting (SLS). In the DNL approach, all parameters

including rate constants and initial concentrations are estimated with a nonlinear solver. In the SLS approach, the inherently linear parameters (concentrations at t_0) and nonlinear parameters (rate constants) are separated and solved in succession.

The concept of separating the nonlinear least squares problem of a physical (hard) model from the linear least squares problem of determining amplitudes has been applied to resolving multicomponent fluorescence spectra from an emission wavelength-decay time data matrix,[20] for resolving overlapped chromatographic peaks in gas chromatography/mass spectroscopy (GC/MS) data[21] and liquid chromatograph/ultraviolet–visible (LC/UV-Vis) data,[22] for resolving multiple components from spectra/pH titration experiments,[23] and most recently for resolving multiple-component adsorption isotherms.[24]

As in soft modeling, only relative concentrations of the spectroscopically distinct species present in these images are generally obtained using these two hard-model approaches. The DNL approach can be applied to reactions of any reaction order while the SLS method is restricted to first-order reactions. The remainder of this paper is focused on describing, applying, and comparing the above mentioned techniques to simulated data and a temporally resolved hyperspectral fluorescence microscope image of fluorescently labeled beads.

For the measured images studied in this paper, the fluorescently labeled beads undergo photobleaching induced by the laser excitation light used by the confocal microscope. We demonstrate our kinetic fitting method by elucidating kinetic models and fitting rate constants to this photobleaching process. It should be noted that time-dependent photobleaching will generally lead to different rates of bleaching for each fluorophore, resulting in the distortion of three-dimensional component maps obtained with the confocal microscope fluorescence microscope. Thus, fitting kinetic models to photobleaching processes may lead to novel methods of correcting photobleaching induced image distortions.

THEORY

The analysis of temporally resolved hyperspectral image data sets is based on the linear additive model expressed in Eq. 1:

$$\mathbf{D}^i_{(m \times n)} = \mathbf{C}^i_{(m \times z)} \mathbf{S}^T_{(z \times n)} + \mathbf{E}^i_{(m \times n)} \tag{1}$$

where $\mathbf{D}^i$ is a matrix of spectra acquired from the ith spatial pixel at m different times and n wavelengths, $\mathbf{C}^i$ is a matrix of pure-component concentration profiles for z species, $\mathbf{S}$ is a matrix of the z pure-component spectra measured at n wavelengths, and $\mathbf{E}$ is the error or residual matrix. For clarity, a definition of all symbols used throughout this section is included in Table I.

There are two main approaches for mathematically resolving the pure-component concentration profiles and pure-component spectral profiles from a temporally resolved multivariate data set. These are denoted as soft-modeling and hard-modeling techniques, and each method has advantages and disadvantages.[25–27]

Soft-modeling methods utilize physically meaningful constraints such as non-negativity in concentration profiles and spectral profiles to obtain physically interpretable pure-component profiles. A soft-modeling method based on MCR-ALS was used in this investigation.[28–30] In MCR-ALS, random numbers are used as initial estimates for the pure-component

TABLE I. Description of symbols used in the Theory section.

Symbol	Description
i	Number of spatial (image) pixels
j	Spectral response index (column of $\mathbf{D}$ or row of $\mathbf{S}$)
m	Number of time points
n	Number of spectral responses (wavelengths)
P	Number of spatial pixels included in the estimate of mean absolute deviation (MAD)
t	Time
z	Number of species
$\mathbf{k}$	Rate constants
$\mathbf{C}^i$	Time-dependent concentration profiles for ith pixel
$\mathbf{c}^i_z$	Time-dependent concentration profile for the zth specie in the ith pixel
$\mathbf{c}^i_0$	Initial concentrations (t_0) for the ith pixel
$\mathbf{D}^i$	Temporally resolved spectral data matrix for the ith pixel
$\mathbf{d}^i_{vec}$	Matrix $\mathbf{D}^i$ vectorized
$\mathbf{E}^i$	Error matrix for the ith pixel
$\mathbf{e}^i_{vec}$	Matrix $\mathbf{E}^i$ stacked into a vector
$\mathbf{F}_z$	Matrix of z basis functions invariant over wavelength
f_z	Basis function describing the zth specie
$\mathbf{S}$	Pure-component spectral matrix
$\boldsymbol{\Phi}_j$	Matrix of z basis functions scaled by the spectral response at wavelength j
$\boldsymbol{\Phi}_{stack}$	Matrix of $\boldsymbol{\Phi}_j$ for all wavelengths stacked on top of each other

spectra, which are then used to estimate the pure-component concentration profiles as shown in Eq. 2:

$$\hat{\mathbf{C}} = \mathbf{D}(\mathbf{S}^T)^+ \tag{2}$$

where $\hat{\mathbf{C}}$ represents the least squares estimate of $\mathbf{C}$ and $(\mathbf{S}^T)^+$ is the pseudo inverse of $\mathbf{S}^T$. The estimated concentration profiles are then used to estimate the pure-component spectra as shown in Eq. 3.

$$\hat{\mathbf{S}}^T = \hat{\mathbf{C}}^+ \mathbf{D} \tag{3}$$

The pure-component concentration profiles and pure-component spectra are then solved in an iterative fashion until a minimum change in the residuals is observed. Non-negativity constraints were applied to the pure-component concentration profiles and pure-component spectra by solving Eqs. 2 and 3 using the fast combinatorial non-negative least squares (fc-nnls) method.[31] In order to obtain kinetic information from the soft-modeling results, model-based concentration profiles are fit to the soft-model estimated concentration profiles.

In hard-modeling methods, pure-component concentration profiles are constrained to strictly follow a specific mechanistic model and nonlinear least squares fitting is used to fit model parameters to experimental data. Traditional kinetic modeling techniques applied to multivariate spectral experiments when initial concentrations of all species are known are well documented in the literature.[32–34]

Hard/soft-modeling algorithms have been developed that attempt to take advantage of the strengths of both hard- and soft-modeling techniques. In hard/soft-modeling, model-based curves are fit to the concentration profiles obtained from Eq. 2 and are subsequently used for solving Eq. 3. These hard/soft-modeling algorithms have been previously described; the reader is referred to the literature for a more in-depth description.[7–9]

Both soft-modeling and hard-modeling techniques can be performed on a single or several temporally resolved multivariate data sets simultaneously, as shown in Fig. 1a. In
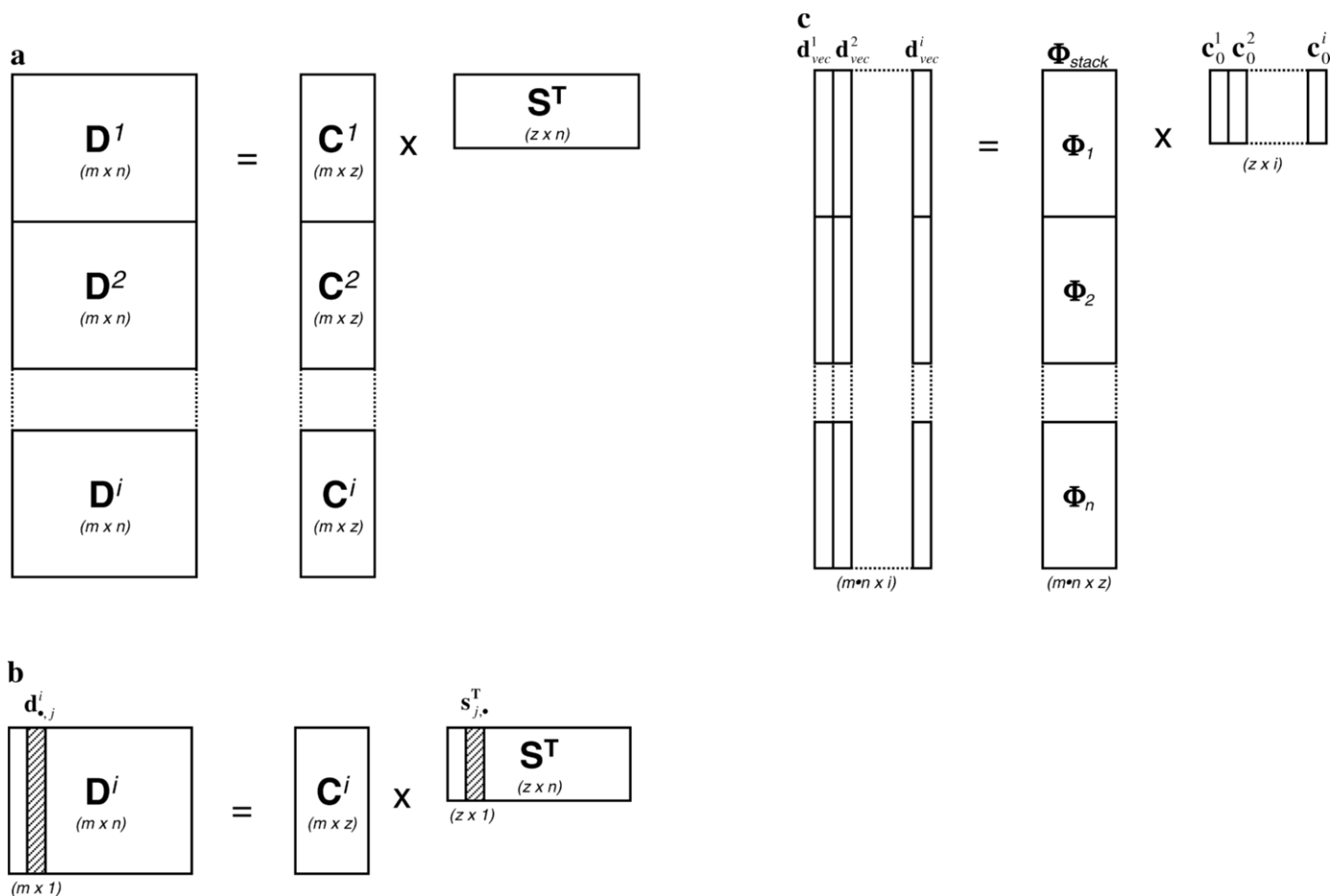
FIG. 1. (a) Linear additive model for the simultaneous analysis of several temporally resolved multivariate data sets. (b) Illustration of analyzing the jth column of $\mathbf{D}$ with the use of Eq. 8. (c) Stacking method for the simultaneous analysis of several temporally resolved multivariate data sets using the SLS approach. Note that the error term is omitted from all figures presented here.

Fig. 1a, each of the matrices $\mathbf{D}^1$, $\mathbf{D}^2$, ..., $\mathbf{D}^i$, represent spectra measured at spatially resolved pixels 1, 2, ..., i as a function of time, and $\mathbf{C}^1$, $\mathbf{C}^2$, ..., $\mathbf{C}^i$ represent the corresponding time-dependent concentration profiles of the z species in each pixel. Using this extended model, Eqs. 2 and 3 are easily applied to several temporally resolved multivariate data sets (pixels) simultaneously. The simultaneous analysis of multiple experiments or multivariate data sets has been shown to be critical for breaking linear dependencies and reducing ambiguities observed in the analysis of single multivariate data sets.[4,10,35] For the simultaneous analysis of multiple pixels we will show in this work that it is possible to model cases in which emitting species have either identical rate constants or identical pure-component spectra as long as (1) the relative concentrations of each emitting specie differ between two or more pixels analyzed and (2) there is sufficient spectral or temporal separation of species. This investigation is focused on kinetic modeling, but it is noteworthy that the spectral modeling algorithms applied to kinetic experiments here may be applied to equilibrium experiments as well.[33]

There are several standard steps in any kinetic modeling procedure. The first step is to postulate a kinetic mechanism. A system of ordinary differential equations (ODE's) is then derived for the proposed model, and for many relatively simple mechanisms, the equations can be explicitly integrated to compute time-dependent concentration profiles. For more complex models, it is necessary to use numerical integration. Concentration profiles can then be computed given initial concentrations and estimates for the model parameters. By fitting the resulting concentration profiles for all apparent species to the spectroscopic measurements, the model parameters may be optimized by standard linear or nonlinear estimation methods as appropriate.[34]

This investigation has focused on the development of the two previously mentioned hard-modeling algorithms (DNL and SLS) in which nonlinear parameters and concentrations at t_0 (i.e., initial concentrations) are optimized simultaneously. In both of these techniques as in soft-modeling, the absolute concentrations cannot be estimated; however, the relative intra-specie concentrations can be obtained, and given the assumption of similar intensity response for all species, relative inter-specie concentrations can be determined. This assumption is implemented in the form of a normalization step, which is necessary to prevent intensity ambiguities in the fitting process that are commonly observed in soft-modeling techniques.[10] The following subsections include in-depth descriptions of the DNL and SLS algorithms. All algorithms were developed and tested using the Matlab® Version 7.4 environment.

Direct Nonlinear Estimation of Initial Concentrations. An initial estimate of the time-dependent concentration profiles, $\mathbf{C}^1$, $\mathbf{C}^2$, ..., $\mathbf{C}^i$, for all i pixels is constructed using a proposed mechanism and an initial "random guess" for the

parameters, e.g., rate constants, $\mathbf{k}$, and concentrations at t_0 for all z species in each pixel, i, $\mathbf{c}_0^1, \mathbf{c}_0^2, \ldots, \mathbf{c}_0^i$. Specific mechanisms and algorithm initializations are discussed in a later section. The estimated concentration profiles are used to estimate the pure-component spectra, $\mathbf{S}$, using the linear least squares estimation step in Eq. 3 extended to several multivariate data sets. The pure-component spectra are then normalized to unit length. The interior-reflective Newton method[36,37] (Matlab® optimization toolbox Version 3.1.1 lsqnonlin.m) of nonlinear estimation is used to estimate the model parameters, $\mathbf{c}_0^1, \mathbf{c}_0^2, \ldots,$ $\mathbf{c}_0^i$, and $\mathbf{k}$, by minimizing Eq. 4:

$$\left\| [(\mathbf{D}^1)^{\mathrm{T}}|(\mathbf{D}^2)^{\mathrm{T}}|\cdots|(\mathbf{D}^i)^{\mathrm{T}}]^{\mathrm{T}} - [(\mathbf{C}^1)^{\mathrm{T}}|(\mathbf{C}^2)^{\mathrm{T}}|\cdots|(\mathbf{C}^i)^{\mathrm{T}}]^{\mathrm{T}}\mathbf{S}^{\mathrm{T}} \right\|$$

(4)

where $\mathbf{C}^i$ represents the time-dependent concentration profiles in the ith pixel for z species such that $\mathbf{C}^i = [\mathbf{c}_1^i \mid \mathbf{c}_2^i \mid \cdots \mid \mathbf{c}_z^i]$, and $\mathbf{c}_z^i = c_{0(z)}^i f_z(k_z, t)$, where $c_{0(z)}^i$ represents the initial concentration of specie z in pixel i and $f_z(k_z, t)$ represents the corresponding kinetic rate law for specie z. By way of example, consider a model for the first-order kinetic decay of $z = 3$ species in an image of $i = 5$ pixels. The resulting model would require fitting $3 \times 5 = 15$ initial concentrations, c_0, and three rate constants, k. The nonlinear fitting method used in this work permits upper or lower bounds to be applied to the model parameters, allowing for easy implementation of non-negativity constraints on the estimated initial concentrations $c_{0(z)}^i$.

Separable Least Squares Estimation of Initial Concentrations. A key feature in the SLS algorithm is the separation of the intrinsically linear parameters, $c_{0(z)}^i$, and nonlinear parameters, k_z. Consider the set of observations, $\mathbf{d}_j^i$, measured over time at wavelength j in pixel i. As shown in Eq. 5, $\mathbf{d}_j^i$ may be approximated by a set of linear parameters $g_1^i, g_2^i, \ldots, g_z^i$ and a set of time-dependent basis functions, $f_1, f_2, \ldots, f_z$, which are dependent on the nonlinear parameters $k_1, k_2, \ldots, k_z$.

$$\mathbf{d}_j^i = g_{j(1)}^i f_1(k_1, t) + g_{j(2)}^i f_2(k_2, t) + \cdots + g_{j(z)}^i f_z(k_z, t) + \mathbf{e}_j^i \quad (5)$$

An error term, $\mathbf{e}_j^i$, is included as well. Defining $\mathbf{g}_j^i = [g_{j(1)}^i \mid g_{j(2)}^i \mid \cdots \mid g_{j(z)}^i]^{\mathrm{T}}$, $\mathbf{k} = [k_1|k_2| \cdots |k_z]$, and $\mathbf{F} = [f_1|f_2| \cdots |f_z]$, Eq. 5 can be re-written in matrix form as shown in Eq. 6, and the linear parameters, $\hat{\mathbf{g}}_j^i$, can be estimated by the linear least squares procedure shown in Eq. 7:

$$\mathbf{d}_j^i = \mathbf{F}(\mathbf{k}, t)\mathbf{g}_j^i + \mathbf{e}_j^i \tag{6}$$

$$\hat{\mathbf{g}}_j^i = \mathbf{F}(\mathbf{k}, t)^+ \mathbf{d}_j^i \tag{7}$$

The nonlinear parameters, $\mathbf{k}$, may be estimated in a separate step with a nonlinear optimization routine by minimizing $\|\mathbf{d}_j^i - \mathbf{F}(\mathbf{k}, t)\mathbf{g}_j^i\|$. The principles of this approach can be applied to any system in which the intrinsically linear and nonlinear parameters are separable.[38]

In this work, SLS is applied specifically to the mechanism of first-order decay. The remainder of this section describes the details of its implementation. A univariate subset of the multivariate linear additive model expressed in Eq. 1 is expressed in Eq. 8 and Fig. 1b for pixel i and wavelength j:

$$\mathbf{d}_j^i = \mathbf{C}^i \mathbf{s}_j^{\mathrm{T}} + \mathbf{e}_j^i \tag{8}$$

where $\mathbf{s}_j$ is the jth row of $\mathbf{S}$. The set of basis functions describing the mechanism of first-order decay is summarized in Eq. 9:

$$\mathbf{F}_{(m \times z)} = [e^{-k_1 t}|e^{-k_2 t}| \cdots |e^{-k_z t}] \tag{9}$$

where k_z represent the first-order decay rates for the z components, respectively. The matrix of concentration profiles, $\mathbf{C}^i$, is obtained from the set of basis functions and the vector of initial concentrations of the z species in pixel i, $\mathbf{c}_0^i$, as shown in Eq. 10:

$$\mathbf{C}_{(m \times z)}^i = \mathbf{F} \, diag(\mathbf{c}_0^i) \tag{10}$$

where $diag(\mathbf{x})$ transforms $\mathbf{x}$ into a square matrix with $\mathbf{x}$ along the diagonal and zeros elsewhere. Substituting Eq. 10 into Eq. 8 gives Eq. 11:

$$\mathbf{d}_j^i = \mathbf{F} \, diag(\mathbf{c}_0^i)\mathbf{s}_j^{\mathrm{T}} + \mathbf{e}_j^i \tag{11}$$

where the product $diag(\mathbf{c}_0^i)\mathbf{s}_j^{\mathrm{T}}$ is analogous to $\mathbf{g}_j^i$ in Eq. 6. Equation 11 may be rearranged into Eq. 12, showing how the linear parameters can be separated from the nonlinear parameters:

$$\mathbf{d}_j^i = \mathbf{F} \, diag(\mathbf{s}_j^{\mathrm{T}})\mathbf{c}_0^i + \mathbf{e}_j^i \tag{12}$$

Defining the matrix $\mathbf{\Phi}_j$ in Eq. 13 allows Eq. 12 to be simplified to Eq. 14:

$$\mathbf{\Phi}_{j(m \times z)} = \mathbf{F} \, diag(\mathbf{s}_j^{\mathrm{T}}) \tag{13}$$

$$\mathbf{d}_j^i = \mathbf{\Phi}_j \mathbf{c}_0^i + \mathbf{e}_j^i \tag{14}$$

The z initial concentrations for pixel i, $\hat{c}_0^i$, are estimated using Eq. 15, which is an applied form of Eq. 7:

$$\hat{\mathbf{c}}_0^i = \mathbf{\Phi}_j^+ \mathbf{d}_j^i \tag{15}$$

The procedure described above for finding the initial concentrations for a temporally resolved univariate data set can be applied to a multivariate data set of time-resolved spectra in the ith pixel by vectorizing $\mathbf{D}^i$ into $\mathbf{d}_{vec(m \cdot n \times 1)}^i$ as shown in Eq. 16:

$$\mathbf{d}_{vec}^i = vec(\mathbf{D}^i) \tag{16}$$

where $vec(\mathbf{X})$ transforms $\mathbf{X}$ into a column vector with one column stacked onto the next. By stacking $\mathbf{\Phi}_j$ for all n wavelengths, we form $\mathbf{\Phi}_{stack}$ as shown in Eq. 17:

$$\mathbf{\Phi}_{stack(m \cdot n \times z)} = [\mathbf{\Phi}_1^{\mathrm{T}}|\mathbf{\Phi}_2^{\mathrm{T}}| \cdots |\mathbf{\Phi}_n^{\mathrm{T}}]^{\mathrm{T}} \tag{17}$$

Substituting the stacked representations into Eq. 13 gives Eq. 18, which is shown as columns in Fig. 1c:

$$\mathbf{d}_{vec}^i = \mathbf{\Phi}_{stack}\mathbf{c}_0^i + \mathbf{e}_{vec}^i \tag{18}$$

Similarly to Eq. 15, the z initial concentrations for the ith pixel are estimated using Eq. 19:

$$\hat{\mathbf{c}}_0^i = \mathbf{\Phi}_{stack}^+ \mathbf{d}_{vec}^i \tag{19}$$

This procedure for separation of the linear and nonlinear parameters may be applied simultaneously to many pixels in a

TABLE II. Description of different parameters used to formulate simulated data sets.

Data set	Spectral correlation coefficient	Rate constants		Number of pixels
		k_1	k_2	
a	1	0.1	0.2	5
b	1	0.1	0.2	500
c	0.7	0.1	0.2	5
d	0.7	0.1	0.2	500
e	0.7	0.5	0.5	5
f	0.7	0.5	0.5	500

temporally resolved hyperspectral image by augmenting data from several pixels as shown in Eq. 20 and Fig. 1c:

$$[\mathbf{d}_{vec}^1|\mathbf{d}_{vec}^2|\cdots|\mathbf{d}_{vec}^i]_{(m\cdot n \times i)} = \mathbf{\Phi}_{stack(m\cdot n \times z)}[\mathbf{c}_0^1|\mathbf{c}_0^2|\cdots|\mathbf{c}_0^i]_{(z \times i)}$$
$$+ [\mathbf{e}_{vec}^1|\mathbf{e}_{vec}^2|\cdots|\mathbf{e}_{vec}^i] \quad (20)$$

where the vectors $\mathbf{d}_{vec}^i$ and $\mathbf{c}_0^i$ correspond to the stacked spectral data and column vector of initial concentrations, respectively, for pixel i. The initial concentrations for all pixels are then estimated using Eq. 21:

$$[\hat{\mathbf{c}}_0^1|\hat{\mathbf{c}}_0^2|\cdots|\hat{\mathbf{c}}_0^i] = \mathbf{\Phi}_{stack}^+[\mathbf{d}_{vec}^1|\mathbf{d}_{vec}^2|\cdots|\mathbf{d}_{vec}^i] \quad (21)$$

In the algorithmic implementation of Eq. 21, a fast combinatorial nonnegative least squares (fc-nnls)[31] method is used to solve for the initial concentrations.

In the algorithmic implementation of SLS, random initial parameter "guesses" are used to construct pure-component concentration profiles for all pixels using Eq. 10. The estimated concentration profiles are then used in Eq. 3 to estimate the pure-component spectra, **S**, which are subsequently used to formulate $\mathbf{\Phi}_{stack}$ as shown in Eqs. 13 and 17. $\mathbf{\Phi}_{stack}$ is used in Eq. 21 to solve for the initial concentrations. The updated estimates for initial concentrations are used in Eq. 10 to construct time-dependent concentration profiles for each pixel. These updated concentration profiles are used in Eq. 3 to obtain new updated pure-component spectral estimates. The estimated pure-component spectra are normalized to unit length, and the corresponding concentration profiles are scaled by the reciprocal of the normalization constant prior the nonlinear optimization step. The nonlinear parameters, i.e., first-order rate constants, are subsequently estimated by the simplex optimization method[39] "fminsearch" from the Matlab® optimization toolbox to minimize Eq. 4. The simplex optimization method was used in this case since it tended to converge smoothly over a wider range of initial estimates compared to other nonlinear least squares methods tested.

EXPERIMENTAL

Data Synthesis and Acquisition. *Simulated Data.* Several simulated data sets were formulated to mimic photobleaching experiments in order to test and compare the performance of the above-mentioned algorithms under ideal conditions. Each simulated data set contained two initial species, *A* and *C*, which followed simple first-order decays producing products *B* and *D*, respectively. Six different data sets were formulated

using different combinations of pure spectra, rate constants, and numbers of pixels. The properties of these simulated data sets were varied to test the algorithms over a variety of conditions including extreme conditions of either identical spectra or identical rate constants. The number of pixels processed was either 5 or 500. The pure-component spectra were either identical or were overlapped with a correlation coefficient of 0.7, and the rate constants, k_1 and k_2, either differed by a factor of two or were identical. The extreme conditions included in these simulated data sets were chosen to illustrate the capability of the DNL and SLS methods to resolve systems with identical rate constants or identical pure-component spectra as long as the relative concentrations of each specie differed between two or more pixels analyzed. The individual properties of each simulated data set are noted in Table II. Time-dependent concentration profiles sampled at 18 equally spaced time intervals of 0.24 ms (integration time for each experimental pixel in the image) were constructed for each pixel using the rate constants specified in Table II and random initial concentrations of *A* and *C*. Simulated pure-component fluorescence spectra spanning the range of 450–700 nm at 0.5 nm increments were formulated by combining Gaussian curves to produce overlapping spectral profiles with the desired correlation coefficient. The simulated pure-component spectra are shown in Fig. 2. The inner product of the desired concentration profiles and pure-component spectra produced the simulated spectral data sets. Poisson noise typical of fluorescence measurements was also added to the data using a pseudo-random Poisson noise generator.[40]

Hyperspectral Bead Data. A temporal hyperspectral fluorescence image of several fluorescently labeled glass beads immobilized in a polymer matrix of polydimethylsiloxane was acquired. The fluorescently labeled beads were prepared by coupling fluorescently labeled streptavidin proteins to functionalized silica microspheres. More details on the bead preparation are available elsewhere.[41] The temporal image of 18 equally spaced time intervals was collected using a hyperspectral confocal microscope developed at Sandia National Laboratories with an oil immersion 60×, NA 1.4 Plan Apochromat objective (Nikon) giving a spatial resolution of 250 nm in the *x* and *y* spatial dimensions.[1]

The image was masked to contain pixels from only two fluorescent beads in order to produce a simplified image. This simplified image included a total of 471 spatial pixels. The goal in reducing the full image to this more simplified image was to provide an experimental data set with a relatively simple first-order photobleaching decay mechanism, which could then be used as a reference for comparing different modeling algorithms applied to an experimental spectral image. The DNL algorithm is limited in the number of pixels that it can analyze because of the computational effort required to estimate large numbers of nonlinear parameters. Therefore, in order to perform DNL fitting on the two-bead image, the image was compressed into five spatially averaged super pixels. The regions averaged for each super pixel and a representative spectrum of each super pixel are included in Figs. 3a and 3b, respectively. Comparisons of raw and super pixels from bead 1 (left bead) and bead 2 (right bead) are included in Figs. 3c and 3d, respectively. There are advantages and disadvantages to analyzing an image compressed by this broad averaging method. Advantages include noise reduction and decreased
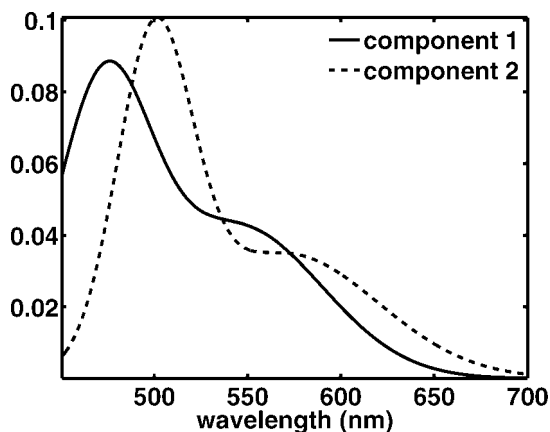
FIG. 2. Simulated fluorescence spectra with correlation coefficient of 0.7.

modeling of all simulated temporally resolved spectral images and the experimental spectral images obtained during photobleaching of the fluorophore-tagged beads. The DNL and SLS algorithms were initialized using a random number generator for the initial estimates of the rate constants and concentrations at t_0 (i.e., initial concentrations). When analyzing simulated data, these algorithms were started at ten different random initializations in order to investigate their convergence properties. The MCR soft-modeling algorithm was initialized using a random number generator for initial estimates of the pure-component spectra. The results from the MCR algorithm were used to initialize the hard/soft-modeling algorithm, and thus computational times required for the soft-modeling are included in the reported hard/soft-modeling analysis time. For all algorithms, non-negativity constraints were imposed on all estimated concentration profiles and pure-component spectra.

Nonlinear solvers such as partial derivative and simplex based methods used in the hard-modeling algorithms are prone to converging to local minima. In order to assure that the hard-modeling algorithms converged completely, the nonlinear least squares optimization routines were restarted until the change in the percent variance explained for consecutive restarts was less than 1×10^{-6}. The percent variance explained

computation time, while a key disadvantage is the possible loss of unique spectral variance due to averaging. The pure-component spectra for such a spatially separated system were readily inferred from the individual beads. All pixels in each spatially separated bead were averaged together to obtain an expected pure-component spectrum for each bead.

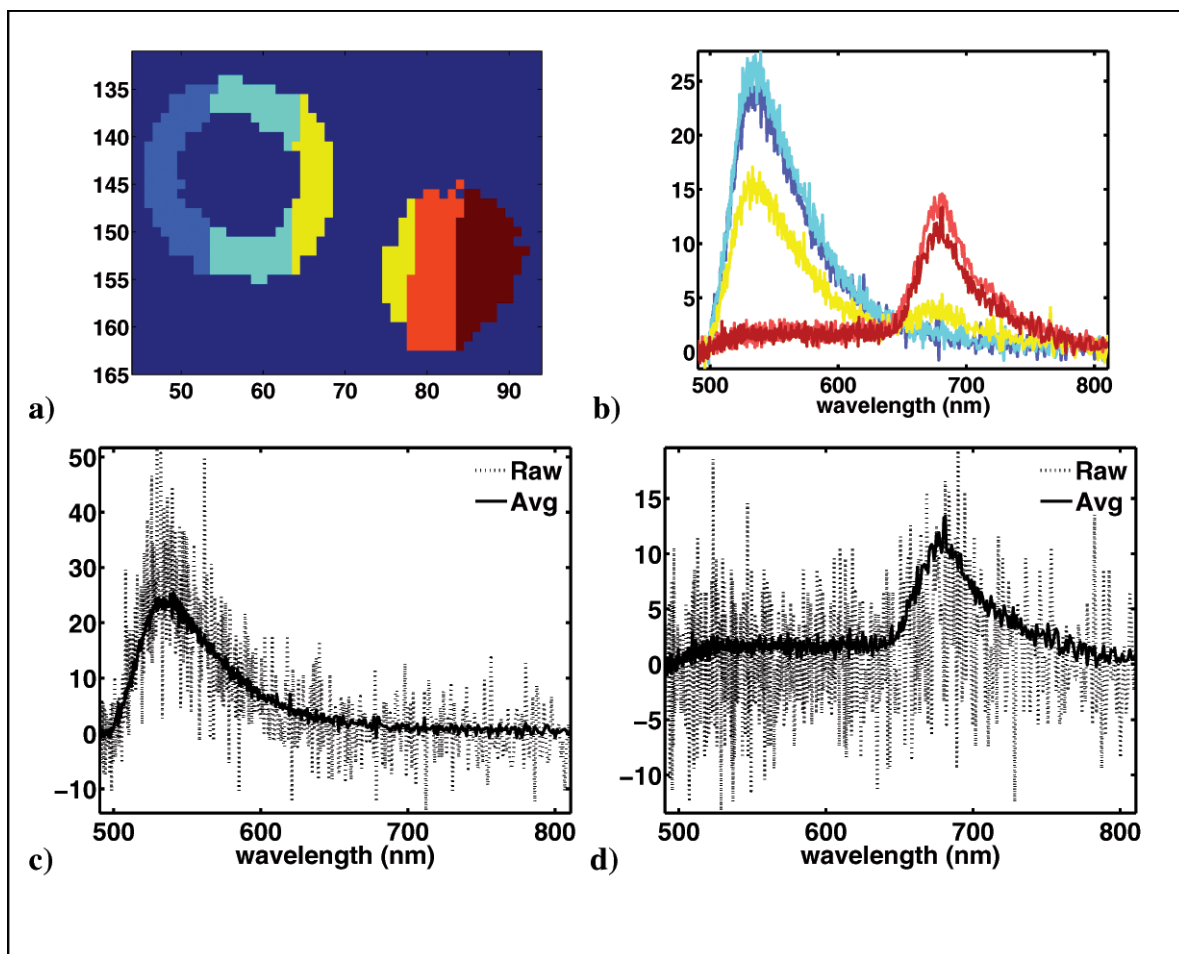**Data Analysis.** Random numbers were used to initialize the

FIG. 3. Experimental bead data. (**a**) Regions averaged into super pixels. (**b**) The initial spectrum of each super pixel. (**c, d**) Raw spectra compared to super pixel spectra of super pixels 1 and 5, respectively.

is shown in Eq. 22:

$$\% \text{ Variance Explained} = 100 \times \frac{\sum\limits_{i,j} \hat{d}_{i,j}^2}{\sum\limits_{i,j} d_{i,j}^2} \qquad (22)$$

where $d_{i,j}$ is an element of the original data set of augmented temporally resolved pixels as shown in Fig. 1a and $\hat{d}_{i,j}$ is an element of that data set reconstructed from the modeling results.

All MCR analyses were performed using principal component analysis (PCA) truncated data as recommended in the original work[10] and terminated when the change in percent variance explained for two consecutive iterations was less than 1×10^{-6}. In order to obtain kinetic rate constants from the soft-modeling results, kinetic concentration profiles were fit to the resultant MCR concentration profiles. All analysis times reported for soft modeling include the time required to fit the kinetic model to the soft-modeled concentration profile. Convergence was considered complete for all hard/soft-modeling analyses when the change in percent variance explained for two consecutive iterations was less than 1×10^{-3}. Differences in the convergence criteria for soft-modeling and hard/soft-modeling are discussed later.

Strict hard-modeling algorithms are often restricted in the number of parameters that can be estimated simultaneously. In a two-component system with 500 pixels, there are 1000 initial concentrations and two rate constants to be estimated. Using the DNL algorithm, all 1002 parameters are estimated simultaneously with a nonlinear solver. The nonlinear solver utilized in the algorithm is not able to estimate such a large number of parameters efficiently; therefore, only the five pixel simulated data sets and experimental data sets with a limited numbers of super pixels were analyzed with the DNL algorithm. Attempts to use the DNL method on 500 pixels resulted in out-of-memory errors when attempting to compute the Hessian matrix (using lsqnonlin solver) on a Windows XP/PC with 4Gb of RAM. It is theoretically possible to use the DNL method with a simplex method (fminsearch), but all attempts failed to converge or were stopped due to extensive computation times (days). Since the SLS algorithm separates the inherently linear parameters (initial concentrations) and inherently nonlinear parameters (rate constants), it is only necessary to estimate two parameters with the nonlinear solver, which improves the algorithm's speed and allows it to be used on much larger data sets.

When super pixels were analyzed with the modeling algorithms, the full image was extrapolated from the space spanned by the modeling results in order to obtain the concentration estimates for every pixel in the image. This extrapolation step differs slightly depending on the algorithm used in the analysis. For soft-modeling, the extrapolation was performed by a simple nonnegative least squares step that estimated temporal concentration profiles for all of the individual pixels in the full image. For the DNL, SLS, and MCR hard/soft-modeling algorithms, the pure-component spectra and rate constants from the kinetic modeling of the super pixels were used to determine temporal concentration profiles for each pixel in the full image. The concentrations extrapolated to the full image were used to compute figures of merit. The time required to extrapolate the fitting results back to the full image is included in the analysis time.

Figures of Merit. Several figures of merit were calculated to compare fitting results from the different algorithms. Some figures of merit are only applicable to the modeling of simulated data sets where the true values of the estimated parameters are known, whereas others are applicable to the modeling of the experimental bead data as well. The percent error in the estimated rate constants and mean average deviation of the estimated initial concentrations are used to characterize the quality of model fit to simulated data sets. The equation for the percent error in the estimated rate constants is shown in Eq. 23:

$$\text{rate constant} (\% \text{ error}) = 100 \times \frac{k - \hat{k}}{k} \qquad (23)$$

where k is the actual rate constant and $\hat{k}$ is the estimated rate constant. The equation for the mean average deviation (MAD) in the estimated concentrations at t_0 is given in Eq. 24:

$$\text{mean average deviation} = \frac{\sum\limits_{i=1}^{p} |c_i - \hat{c}_i|}{p} \qquad (24)$$

where c_i is the actual concentration at t_0 for pixel i for a given specie, $\hat{c}_i$ is the corresponding estimated initial concentration, and p is the number of pixels included in the modeling.

The lack of fit (LOF) in the pure-component spectra is used to show the accuracy of the model-estimated spectra compared to the actual or expected values. The formula for the spectral lack of fit is presented in Eq. 25:

$$\text{spectral lack of fit} (\%) = 100 \times \sqrt{\frac{\sum\limits_{j=1}^{n} (s_j - \hat{s}_j)^2}{\sum\limits_{j=1}^{n} s_j^2}} \qquad (25)$$

where s_j is the actual or expected pure-component spectrum at wavelength j, $\hat{s}_j$ is the estimated pure-component spectrum, and n is the number of spectral wavelengths included in the modeling.

The root mean squared error (RMSE) is used as a figure of merit to evaluate the overall quality of a fit. This value is computed as shown in Eq. 26:

$$\text{RMSE} = \sqrt{\frac{\sum\limits_{i,j} (d_{i,j} - \hat{d}_{i,j})^2}{n_{rows} n_{cols}}} \qquad (26)$$

where $d_{i,j}$ is an element of the original spectral data set of stacked pixel data measured over time as shown in Fig. 1a, $\hat{d}_{i,j}$ is the element in the ith row and jth column of the data set reconstructed from the modeling results, n_{rows} is the number of rows (number of pixels times number of time points) in the data set, and n_{cols} is the number of columns (spectral wavelengths) in the data set. Two values are presented for the RMSE for simulated data with Poisson noise added. The "Model Estimated" is calculated as described above, and the "Actual"

column is calculated by substituting the noise free simulated data for $\hat{d}_{i,j}$ in Eq. 19.

RESULTS AND DISCUSSION

Kinetic Modeling of Simulated Data. When modeling multivariate data with methods based on first principles models like SLS and DNL, it is possible to fit a wide range of different mechanisms; thus, it is important to have the ability to discern between several different plausible models. This ability to distinguish between models was tested during the developmental phase of the DNL algorithm where the DNL approach was applied to simulated spectral image data similar to that presented here. For example, it is possible to fit models such as $2A \xrightarrow{k_1} B$ and $2C \xrightarrow{k_2} D$ using the DNL method. It is beyond the scope of this work to show the exhaustive sets of results that were obtained with numerous different models; however, it should be sufficient to note that in all cases the most parsimonious and statistically sufficient models were those corresponding to the true simulated models. For this reason, only the two-component first-order decay results are discussed here. The SLS algorithm is limited in its ability to test different models since it is only applicable to models containing inherently linear and nonlinear parameters that can be separated.

Kinetic Modeling of Noise-Free Simulated Data. The simulated data sets with and without added Poisson noise were analyzed with the hard-modeling, soft-modeling, and hard/soft-modeling algorithms. The noise-free simulated data sets were analyzed in order to test each algorithm on ideal data. The kinetic modeling results and associated figures of merit for the noise-free data sets are shown in Table III. The DNL results for data sets b, d, and f (data sets with 500 pixels each) are omitted in Table III because of "out of memory errors". It was previously noted that the DNL algorithm performed poorly in these kinds of situations, and it was this poor performance that provided the initial motivation to pursue the development of the alternate SLS algorithm. The soft-modeling and hard/soft-modeling results for data sets a and b are omitted in Table III because the algorithm produced rank deficiency errors when computing the matrix inverse of $\mathbf{S}^T$ due to identical pure-component spectra of constituents A and C. Inspecting the figures of merit noted in Table III, it is apparent that the hard-modeling and hard/soft-modeling algorithms yield significantly better results than the soft-modeling algorithm. The DNL and SLS hard-modeling algorithms perform slightly better than the hard/soft-modeling algorithm. The DNL algorithm performed much more slowly than the other algorithms, whereas the SLS algorithm had the fastest analysis times.

The DNL and SLS algorithms were randomly initialized 10 times. It is well known that the convergence of many nonlinear fitting problems can be heavily dependent on the quality of the starting values; thus, the number of trials that successfully converged using random starting values is shown in Table III as a rough indicator of the convergence properties and robustness of the method. In some cases, very poor initial guesses of the parameters can lead to negative estimates of initial concentrations, which are in turn forced to zero by the non-negativity constraints, resulting in rank deficiency in Φ_{stack}. Due to the extreme cases tested with noise-free data (i.e., identical pure-component spectra or identical rate constants) a number of pathological cases (convergence failures) were observed and are noted in Table III. The result

of the first random initialization to converge is presented in Table III. All random initializations of the DNL algorithm for data sets a and c yielded reasonable parameter estimates similar to the known true values (e.g., similar rate constants, initial concentrations, pure-component spectra, and RMSE). For data sets a through d, the SLS algorithm either converged to results with consistent figures of merit similar to truth or exited immediately due to a rank deficiency in Φ_{stack} when solving for the initial concentrations (see Eq. 21). For the hard-modeling analyses of data sets e and f, the same convergence trends were observed as in data sets a through d except for a higher MAD for initial concentrations and larger lack of fit in the pure-component spectra. These poorer results are due to the identical rate constants in data sets e and f, and they indicate that there is insufficient selectivity in these particular simulated data sets to fully resolve both species.

As stated previously, the noise-free data sets with identical spectra (data sets a and b) could not be modeled using the soft-modeling or hard/soft-modeling algorithms because the spectral matrix is rank deficient. The SLS algorithm is able to overcome this rank deficiency due to Eq. 13 in which the pure-component spectra are combined with the set of basis functions describing the concentration profiles. The spectral matrix is not inverted in either the SLS or DNL algorithms; therefore, they are unaffected by a rank deficient spectral matrix.

The convergence criteria initially used for the hard/soft-modeling of noise-free simulated data was a 1×10^{-6} change in percent variance explained. When this convergence criteria was used, over-fitting was often observed, which resulted in divergence from the minimum RMSE. Inspection of intermediate results during the operation of this algorithm revealed that use of direct substitution of the kinetic concentration profiles caused this divergent behavior. When the convergence criterion was changed to 1×10^{-3} change in percent variance explained, the algorithm yielded reasonable parameter estimates similar to the known true values as shown in Table III.

Kinetic Modeling of Simulated Data with Added Poisson Noise. Modeling of noise-free data demonstrates how the algorithms perform in ideal cases. Table IV, which presents the results of modeling of simulated data with added Poisson noise, is critical for understanding how these algorithms perform under more realistic circumstances. Comparison of the model-estimated RMSE with the actual RMSE reveals excellent results in all cases but one.

The hard-modeling algorithms were randomly initialized ten times. All random initializations of the DNL algorithm behaved similar to the noise-free data. The rank deficiency affecting the SLS algorithm in the noise-free data was less prevalent in the noisy data because the Poisson noise helps to break the rank deficiency when very poor initial estimates are used. As with the noise-free simulated data, the first random initialization to converge is reported in Table IV and the number of trials that successfully converged is shown in the last column.

Several trends are apparent from the hard-modeling results shown in Table IV. The DNL and SLS algorithms yield comparable results, but the SLS algorithm is at least ten times faster in all instances and is able to analyze much larger data sets. It is clear that when using SLS, the analysis of the larger data sets (500 pixels versus 5 pixels) yielded significantly better fitting results. Similar improvements in the results with the larger data sets were not found for the MCR soft-modeling or

TABLE III. Results from kinetic modeling of noise-free simulated data.

Data set	Rate constants (% error)	Initial concentration (t_0) Mean	Initial concentration (t_0) MAD	Spectra (% LOF)	RMSE Actual	RMSE Model estimated	Analysis time (s)	Number of trials converged
DNL								
a	1.0	393.4	8.3	0.0	0.00	0.00	1547	2
	0.5	480.0	8.3	0.0				
c	−0.1	393.4	0.8	0.0	0.00	0.00	2333	1
	0.0	480.0	0.8	0.0				
e	0.0	393.4	107.8	6.6	0.00	0.00	1079	6
	0.0	480.0	108.6	6.1				
SLS								
a[a]	0.0	393.4	0.6	0.0	0.00	0.00	1	9
	0.1	480.0	0.6	0.0				
b[a]	0.0	349.2	0.2	0.0	0.00	0.00	45	10
	0.1	335.2	0.3	0.0				
c	−0.1	393.4	1.4	0.1	0.00	0.00	4	7
	−0.1	480.0	1.4	0.1				
d	0.0	349.2	0.0	0.0	0.00	0.00	365	5
	0.0	335.2	0.0	0.0				
e	0.0	393.4	102.8	6.3	0.00	0.00	1	5
	0.0	480.0	103.5	5.8				
f	0.0	349.2	35.5	0.1	0.00	0.00	221	4
	0.0	335.2	30.3	5.8				
MCR								
c	−1.4	393.4	91.0	19.6	0.00	0.03	6	NA
	10.4	480.0	113.3	0.9				
d	0.6	349.2	90.3	19.5	0.00	0.03	610	NA
	11.9	335.2	107.7	0.6				
e	0.0	393.4	81.9	20.0	0.00	0.02	5	NA
	0.0	480.0	107.3	2.0				
f	0.0	349.2	82.8	19.0	0.00	0.02	623	NA
	0.0	335.2	101.0	0.5				
MCR hard/soft								
c	−3.9	393.4	19.2	5.1	0.00	0.23	9	NA
	3.7	480.0	25.3	2.4				
d	1.9	349.2	34.5	4.3	0.00	0.11	955	NA
	3.6	335.2	37.0	1.3				
e	0.0	393.4	81.9	19.9	0.00	0.02	5	NA
	0.0	480.0	107.1	2.0				
f	0.0	349.2	82.7	18.9	0.00	0.02	668	NA
	0.0	335.2	100.8	0.5				

[a] With identical spectra and noise free data, non-negativity had to be turned off for the estimation of concentrations at t_0.

hard/soft modeling methods. In comparing the MCR soft-modeling and hard/soft-modeling results, the implementation of the kinetic constraints improved the fitting results in most cases. For both MCR soft-modeling and hard/soft-modeling, inaccurate results were obtained for data sets with identical pure spectra (data sets a and b) because of rank deficiencies in the spectral matrix. Also, an improvement in the spectral lack of fit was not observed as the number of pixels analyzed increases.

The SLS modeling algorithm was generally comparable to the MCR hard/soft-modeling algorithms when comparing the metric of percent error in the rate constants. The SLS algorithm often outperformed the MCR hard/soft-modeling algorithm in the MAD of initial concentrations and the spectral lack of fit metrics. The analysis times were mostly comparable for the 5 pixel data sets, but exhibited a large advantage in two of the three analyses with the 500 pixels.

Analysis of Experimental Temporal Hyperspectral Fluorescence Bead Data. The results from the temporal hyperspectral bead data analyzed with the DNL, SLS, soft-modeling, and hard/soft-modeling algorithms, are presented in Table V. The two beads were assumed to each contain a different single fluorescence component and were spatially resolved in the image. Thus, the true pure-component spectrum

of each fluorophore could be estimated from the average spectrum of each bead. These estimated pure spectra were then used for estimating the spectral lack of fit for the model-estimated spectra presented in Table V. The data set denoted as "Avg" is the set of five super pixels, and the data set denoted as "Raw" is the entire two-bead image (471 selected spatial pixels). The first-order kinetic model and several different two-component second-order decay mechanisms were fit to the super pixels using the DNL algorithm. The two-component first-order decay mechanism is the most parsimonious and statistically sufficient mechanism for the two-bead image; therefore, only the results from analyses using this mechanism are presented.

As in the kinetic modeling of the simulated data, the SLS and DNL results are in good agreement. Similar rate constants are obtained from the soft-modeling and hard/soft-modeling results, but the spectral lack of fit for bead 2 is somewhat greater than expected based on the results obtained from the DNL and SLS hard-model analyses when the rate constants differ by a factor of 2. These results do not follow the trends observed in the simulated data.

The observed differences in the trends in spectral lack of fit between the experimental and simulated data led to additional

TABLE IV. Results from the kinetic modeling of simulated data with noise added.

Data set	Rate constants (% error)	Initial concentration (t_0)		Spectra (% LOF)	RMSE		Analysis time (s)	Number of trials converged
		Mean	MAD		Actual	Model estimated		
DNL								
a	50.9	393.4	76.9	8.8	4.76	4.69	366	2
	−28.1	480.0	83.2	9.1				
c	−13.4	393.4	85.9	6.7	4.74	4.69	357	1
	−3.9	480.0	86.1	6.6				
e	−0.6	393.4	110.4	9.0	3.63	3.56	252	6
	1.1	480.0	109.4	9.8				
SLS								
a[a]	24.5	393.4	130.2	6.6	4.76	4.69	4	9
	−47.6	480.0	123.5	12.2				
b[a]	1.9	349.2	11.7	0.5	4.21	4.21	53	10
	−1.0	335.2	13.8	0.6				
c	−9.5	393.4	49.4	5.3	4.74	4.69	4	7
	−1.7	480.0	49.0	5.3				
d	0.1	349.2	2.6	0.5	4.22	4.22	284	5
	−0.2	335.2	3.3	0.6				
e	−0.9	393.4	40.2	9.0	3.63	3.56	20	5
	0.9	480.0	36.7	7.7				
f	0.1	349.2	30.5	1.1	3.20	3.20	367	4
	−0.1	335.2	25.0	5.7				
MCR								
a	−20.9	393.4	129.0	29.1	4.76	4.63	3	NA
	7.0	480.0	130.1	29.5				
b	−46.4	349.2	111.7	29.1	4.21	4.19	252	NA
	26.8	335.2	111.4	29.3				
c	−7.6	393.4	71.4	14.6	4.74	4.67	7	NA
	10.6	480.0	80.5	4.5				
d	−3.3	349.2	70.6	19.1	4.22	4.21	540	NA
	11.8	335.2	91.0	2.6				
e	−1.1	393.4	44.0	12.9	3.63	3.55	6	NA
	0.3	480.0	55.5	6.4				
f	0.5	349.2	59.0	19.5	3.20	3.19	283	NA
	−0.5	335.2	82.7	5.5				
MCR hard/soft								
a	−33.7	393.4	159.6	19.8	4.76	4.79	4	NA
	12.1	480.0	162.4	21.9				
b	−312.6	349.2	327.1	0.4	4.21	10.30	3678	NA
	−98.5	335.2	327.0	0.4				
c	−1.9	393.4	49.2	5.1	4.74	4.71	8	NA
	4.1	480.0	40.0	5.5				
d	−6.7	349.2	22.2	4.2	4.22	4.24	802	NA
	3.6	335.2	20.1	5.6				
e	−1.1	393.4	44.9	11.6	3.63	3.57	7	NA
	0.3	480.0	53.3	6.1				
f	0.5	349.2	59.8	19.2	3.20	3.21	319	NA
	−0.5	335.2	82.9	5.1				

[a] Non-negativity turned off for the estimation of concentrations at t_0 for comparison with Table III.

evaluations of the experimental data. Upon further investigation with both PCA and the kinetic modeling of each bead separately, we found evidence of a second very weak fluorophore in bead 2 (bead to the lower right in Fig. 3a) that has an emission spectrum similar to the fluorophore in bead 1. The presence of a second fluorophore in bead 2 could either be due to experimental contamination of bead 2 or more likely due to a small amount of spectral bleed-through of emission from another bead above or below bead 2. Therefore, our presumption that the average spectrum from bead 2 represents the pure spectrum of the fluorophore is not completely accurate. Thus, we have some unknown amount of error in the pure spectrum of bead 2, and our spectral lack of fit metric for this fluorophore cannot be considered accurate in Table V. The spectral lack of fit metric should be valid for the fluorophore in bead 1, and the trends in the experimental data for this bead are consistent with those of the simulated data.

This experimental example points out the need to always validate the assumptions in the experimental data through a careful examination and analysis of the data. Although this supposedly simplistic two-bead image does not allow a full evaluation and comparison of the different modeling approaches, it does help to demonstrate the use of the SLS and DNL approaches in comparison with soft and hard/soft models applied to real experimental temporally resolved hyperspectral fluorescence image data.

CONCLUSION

Fitting of temporally resolved hyperspectral fluorescence images by kinetic modeling offers greater accuracy and precision compared to soft-modeling and hard/soft-modeling as shown in Tables III, IV, and V. We have found that the SLS algorithm offers significant advantages over the DNL method

TABLE V. Results from kinetic modeling of experimental bead data.

Data set	Bead	k (ms^{-1})	Spectra (% LOF)	RMSE	Analysis time (s)
DNL					
Avg	Bead 2	0.37	10.1	6.23	1501
	Bead 1	0.21	3.9		
SLS					
Avg	Bead 2	0.37	10.1	6.23	1
	Bead 1	0.21	3.9		
Raw	Bead 2	0.36	14.6	6.23	38
	Bead 1	0.21	4.3		
Soft					
Avg	Bead 2	0.39	20.1	6.42	14
	Bead 1	0.22	4.8		
Raw	Bead 2	0.41	20.1	6.09	107
	Bead 1	0.25	4.8		
Hard/soft					
Avg	Bead 2	0.40	26.1	6.42	14
	Bead 1	0.22	4.0		
Raw	Bead 2	0.41	26.1	6.42	153
	Bead 1	0.25	4.9		

since SLS is much faster and it is not as limited in the number of pixels that can be analyzed simultaneously. On the other hand, DNL has the advantage that it can be applied to higher order kinetic models. We also demonstrated that simultaneous fitting of a single kinetic model to many image pixels reduces ambiguity in the estimated parameters, reduces the impact of measurement noise, and allows more reliable fitting of complex models with a combination of many linear parameters (concentration at t_0) and a few nonlinear parameters (rate constants). The two major challenges of fitting kinetic models to temporally resolved hyperspectral images (estimating concentrations at t_0 and large number of pixels) can be effectively overcome by the use of the SLS method as shown in this paper. Although only applicable to first-order decay such as photobleaching experiments, these kinds of experiments represent a major application area of temporally resolved hyperspectral images and thus represent a significant technological advance.

The aim of future work is to apply the SLS method in obtaining kinetic information (rate constants) for temporally resolved hyperspectral images of real biological samples, with the long-term goal of correcting the effects of photobleaching in hyperspectral images with three spatial dimensions.

1. M. B. Sinclair, D. M. Haaland, J. A. Timlin, and H. D. T. Jones, Appl. Opt. **45,** 6283 (2006).
2. J. R. Schoonover, R. Marx, and S. L. Zhang, Appl. Spectrosc. **57,** 154A (2003).
3. S. Bijlsma, H. F. M. Boelens, H. C. J. Hoefsloot, and A. K. Smilde, J. Chemom. **16,** 28 (2002).
4. P. Bugnon, J.-C. Chottard, J.-L. Jestin, B. Jung, G. Laurenczy, M. Maeder, A. E. Merbach, and A. D. Zuberbuhler, Anal. Chim. Acta **298,** 193 (1994).
5. J. R. Knutson, J. M. Beechem, and L. Brand, Chem. Phys. Lett. **102,** 501 (1983).
6. M. Maeder and A. D. Zuberbuehler, Anal. Chem. **62,** 2220 (1990).
7. E. Bezemer and S. C. Rutan, Chemom. Intell. Lab. Syst. **59,** 19 (2001).
8. A. de Juan, M. Maeder, M. Martinez, and R. Tauler, Chemom. Intell. Lab. Syst. **54,** 123 (2000).
9. A. de Juan, M. Maeder, M. Martinez, and R. Tauler, Anal. Chim. Acta **442,** 337 (2001).
10. R. Tauler, A. Smilde, and B. Kowalski, J. Chemom. **9,** 31 (1995).
11. M. Ehly, P. J. Gemperline, A. Nordon, D. Littlejohn, J. K. Basford, and M. De Cecco, Anal. Chim. Acta **595,** 80 (2007).
12. E. Furusjo, O. Svensson, and L.-G. Danielsson, Chemom. Intell. Lab. Syst. **66,** 1 (2003).
13. P. Gemperline, G. Puxty, M. Maeder, D. Walker, F. Tarczynski, and M. Bosserman, Anal. Chem. **76,** 2575 (2004).
14. D. Chatterjee, M. S. A. Hamza, M. M. Shoukry, A. Mitra, S. Deshmukh, and R. van Eldik, Dalton Trans., 2, 203 (2003).
15. P. G. Lye, G. A. Lawrance, and M. Maeder, J. Chem. Soc., Dalton Trans. **16,** 2376 (2001).
16. M. Maeder, Y.-M. Neuhold, G. Puxty, and P. King, Phys. Chem. Chem. Phys. **5,** 2836 (2003).
17. N. McCann, G. A. Lawrance, Y. M. Neuhold, and M. Maeder, Inorg. Chem. **46,** 4002 (2007).
18. S. Yamada, T. Kido, and M. Tanaka, Inorg. Chem. **23,** 2990 (1984).
19. L. Balland, N. Mouhab, J. M. Cosmao, and L. Estel, Chem. Eng. Proc. **41,** 395 (2002).
20. F. J. Knorr and J. M. Harris, Anal. Chem. **53,** 272 (1981).
21. F. J. Knorr, H. R. Thorsheim, and J. M. Harris, Anal. Chem. **53,** 821 (1981).
22. S. D. Frans, M. L. McConnell, and J. M. Harris, Anal. Chem. **57,** 1552 (1985).
23. S. D. Frans and J. M. Harris, Anal. Chem. **56,** 466 (1984).
24. D. Rivera, P. E. Poston, R. H. Uibel, and J. M. Harris, Anal. Chem. **72,** 1543 (2000).
25. M. S. Diaz-Cruz, J. M. Diaz-Cruz, J. Mendieta, R. Tauler, and M. Esteban, Anal. Biochem. **279,** 189 (2000).
26. R. M. Dyson, M. Hazenkamp, K. Kaufmann, M. Maeder, M. Studer, and A. Zilian, J. Chemom. **14,** 737 (2000).
27. R. M. Dyson, P. Jandanklang, M. Maeder, C. J. Mason, and A. Whitson, Polyhedron **18,** 3227 (1999).
28. R. Bro and S. De Jong, J. Chemom. **11,** 393 (1997).
29. D. M. Haaland, J. A. Timlin, M. B. Sinclair, M. H. Van Benthem, M. J. Martinez, A. D. Aragon, and M. Werner-Washburne, "Multivariate curve resolution for hyperspectral image analysis: applications to microarray technology", in *Spectral Imaging: Instrumentation, Applications, and Analysis II* (SPIE, San Jose, CA, 2003), p. 55.
30. P. G. Kotula, M. R. Keenan, and J. R. Michael, Microsc. Microanal. **9,** 1 (2003).
31. M. H. Van Benthem and M. R. Keenan, J. Chemom. **18,** 441 (2004).
32. S. Bijlsma, H. F. M. Boelens, H. C. J. Hoefsloot, and A. K. Smilde, Anal. Chim. Acta **419,** 197 (2000).
33. S. Norman and M. Maeder, Crit. Rev. Anal. Chem. **36,** 199 (2006).
34. G. Puxty, M. Maeder, and K. Hungerbuhler, Chemom. Intell. Lab. Syst. **81,** 149 (2006).
35. R. M. Dyson, S. Kaderli, G. A. Lawrance, and M. Maeder, Anal. Chim. Acta **353,** 381 (1997).
36. T. F. Coleman and Y. Li, Math. Prog. **67,** 189 (1994).
37. T. F. Coleman and Y. Li, SIAM J. Opt. **6,** 418 (1996).
38. H. B. Nielsen, "Separable NonLinear Least Squares", in *Report IMM-REP-2000* (2000), p. 16.
39. C. L. Jeffrey, A. R. James, H. W. Margaret, and E. W. Paul, SIAM J. Opt. **9,** 112 (1998).
40. L. Debroye, *Non-Uniform Random Variate Generation* (Springer-Verlag, New York, 1986).
41. D. M. Haaland, M. B. Sinclair, H. D. T. Jones, J. A. Timlin, L. T. Nieman, G. D. Bachand, D. Y. Sasaki, G. S. Davidson, and M. H. V. Benthem, "3D Optical Sectioning with a New Hyperspectral Confocal Fluorescence Imaging System", in *Sandia Report* (Sandia National Laboratories, Albuquerque, NM and Livermore, CA, 2007).